



# Kinetics and mechanisms of the carbothermic reduction of chromite in the presence of nickel

Dawei Yu<sup>1</sup> · Dogan Paktunc<sup>1</sup>

Received: 13 September 2017 / Accepted: 15 December 2017 / Published online: 11 January 2018  
© Crown 2018

## Abstract

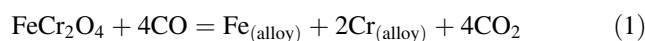
Carbothermic reduction of chromite in the presence of nickel as the alloying element was investigated in a wide temperature range up to 1500 °C using thermogravimetric analysis coupled with continuous off-gas analysis (TG-DSC-MS). Both isothermal and non-isothermal linear heating tests were performed for the kinetic study with the calculation of activation energies. In order to further elucidate the reduction mechanism, the reduced products were characterized by SEM–EDS and XRD. It was concluded that the reduction sequence followed a multi-stage mechanism, reflected partly by the dependency of the activation energy on the extent of reduction. With the progress of reduction, refractory oxide layers gradually formed on/close to the surface of each chromite particle, causing the shift of the rate-limiting factor from chemical control to diffusion control. The promoting effect from the addition of Ni was evident at temperatures higher than 1300 °C due to the formation of alloys of lower melting point.

**Keywords** Chromite · Ferrochrome · Carbothermic reduction · Alloying · Kinetics

## Introduction

Chromium is an essential alloying element for the production of stainless and high-alloy ferritic steels. The production of chromium mainly in the form of ferrochromium (FeCr) alloys is dominantly performed by smelting chromite in submerged arc furnaces (SAF) [1]. Approximately 80% of the FeCr (primarily as high-carbon or charge grade) produced is consumed in the stainless steel industry [2]. SAF smelting operation is highly electric-energy intensive, consuming electricity of about 2.4 to 4.8 MWh tonne<sup>-1</sup> FeCr [3]. Although SAF smelting of chromite is a mature technology where improvement to reduce the production cost is more difficult [1], significant technological and research efforts and improvements have been made to further reduce the energy cost of FeCr production, especially in the area of solid-state carbothermic pre-reduction of chromite, which could potentially reduce the power consumption of the SAF process [4].

Chromite is a spinel mineral containing Mg, Al, Fe and Cr in varying proportions according to its formula (Mg, Fe<sup>2+</sup>)(Cr, Al, Fe<sup>3+</sup>)<sub>2</sub>O<sub>4</sub> [2]. It is considered as a difficult oxide for recovering Cr. Carbothermic reduction of chromite can be represented by Reaction Eqs. 1 to 3. The relatively refractory components (i.e., Mg and Al in the form of oxides) remain as oxide(s) after reduction. Given the condition that finely distributed carbon is in close proximity to chromite, CO could possibly become the principal reducing agent, represented by Reaction Eqs. 1 and 2 [5]. Gasification of carbon via Reaction 2 (i.e., reversed Boudouard reaction) quickly restores the low local oxygen partial pressure by consuming CO<sub>2</sub> produced from Reaction 1 and regenerating CO, allowing Reaction 1 to continue. Reaction Eqs. 1 and 2 represent the indirect reduction of chromite, which was suggested to be of much more significance compared to direct reduction by solid carbon via Reaction Eq. 3 [5].



✉ Dawei Yu  
dawei.yu@hotmail.com

<sup>1</sup> CanmetMINING, Natural Resources Canada, 555 Booth Street, Ottawa, ON K1A 0G1, Canada

Numerous studies focusing on the kinetics and mechanisms of carbothermic reduction of natural or synthetic chromite were conducted [4–15]. Based on previous investigations, Wang et al. [12] summarized various rate-controlling mechanisms and their apparent activation energies for the carbothermic reduction of chromite with and without additives. A multi-stage mechanism was proposed by most researchers based on this summary. In general, the early stage tends to be controlled by nucleation or chemical reactions, and the late stage is most likely controlled by diffusion, with activation energies reported ranging from 57 up to 410 kJ mol<sup>-1</sup>. The later stage diffusion-controlled mechanism is likely to be caused by the gradual formation of a very stable picrochromite-spinel solid solution (MgO(Cr,Al)<sub>2</sub>O<sub>3</sub>) at the surface of each chromite grain [16, 17].

The approaches for enhancing the chromite reduction can be generally classified into four categories by addressing the above-mentioned kinetic limitations.

- (1) Pre-treatment of chromite to enhance its reactivity before reduction, including pre-oxidation or heat treatment [18–20], and mechanical activation of chromite by high-energy milling [21].
- (2) Addition of slag-making fluxes, such as CaF<sub>2</sub> [17], SiO<sub>2</sub> [22–26], CaO [20], K<sub>2</sub>CO<sub>3</sub>, Na<sub>2</sub>O<sub>2</sub> [27], NaF-CaF<sub>2</sub>, fluorspar-feldspar-silica and fluorspar-granite [16].
- (3) Addition of alloying elements, or in situ formation of alloying elements, such as the addition of iron powder [28, 29], mill scale (FeO<sub>x</sub>) [30], Cr [27], and nickel laterite ore [31].
- (4) Addition of reagents that promotes the Boudouard reaction (i.e., Reaction 2). According to Katayama et al. [32], addition of sodium borate (Na<sub>2</sub>B<sub>4</sub>O<sub>7</sub>) or NaCl improves chromite reduction by promoting the Boudouard reaction. Van Deventer [27] reported that SiO<sub>2</sub>, Al<sub>2</sub>O<sub>3</sub>, K<sub>2</sub>CO<sub>3</sub>, Na<sub>2</sub>O<sub>2</sub>, CaO, MgO, Fe and Cr positively influenced the Boudouard reaction.

By adopting the third approach, Ni powder was used as the alloying element for promoting the carbothermic solid reduction of chromite. There are three main reasons for using Ni powder as the alloying element. Firstly, similar to Cr, Ni is also a critical alloying element for making stainless steels of most grades. Therefore, Cr–Ni–Fe alloys produced from chromite reduction can be used in the production of stainless steel. Secondly, addition of Ni powder could potentially reduce the activity of the *as-formed* Cr and Fe, thereby accelerating the chromite reduction. Thirdly, the presence of Ni could lower the temperature at which molten alloys start to form, which in

turn promote the reduction kinetics by lowering the mass transfer limitations. Using FactSage [33], a phase diagram of the Cr–Fe–Ni–C system was generated by fixing the carbon content at 10 mass% and mass ratio of Cr:Fe at 2 (Fig. 1). As illustrated, when the mass ratio of Ni/(Cr + Fe + C) is above approximately 0.1, the temperature at which liquid alloys start to form is at about 1200 °C, which is 300 °C lower compared to the case in which no Ni is added (> 1500 °C).

The influence of Ni or NiO addition on the smelting reduction of chromite fluxed with SiO<sub>2</sub> and CaO has been previously investigated at 1550 and 1650 °C [34], which demonstrates the feasibility of directly producing a high-carbon ferrochromium-nickel alloy suitable for stainless steel production. In our study, the influence of Ni addition was evaluated at the solid reduction regime at a lower operating temperature (≤ 1500 °C) in the absence of fluxes, which could potentially reduce the energy cost and the amount of slag waste generation associated with ferrochrome production. The formation of liquid alloy at a much lower temperature could potentially promote the alloy growth, which facilitates the subsequent separation of alloy from the unwanted gangue without the need of SAF. By employing the thermogravimetric analysis in combination with the characterization of the products, kinetics and mechanisms of chromite reduction were investigated with or without the addition of Ni.

## Materials and methods

### Materials

The as-received chromite ore was sieved, and the size fraction of 75–105 μm was used for the experiments.

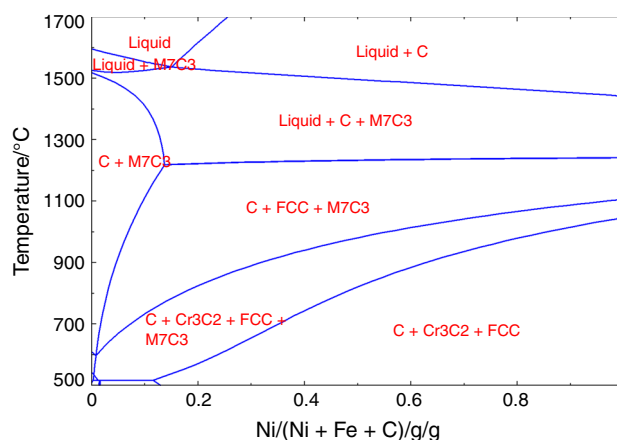


Fig. 1 Cr–Fe–Ni–C system as a function of temperature and Ni content, generated using FactSage [33]

**Table 1** Composition of the chromite ore (mass%)

Cr <sub>2</sub> O <sub>3</sub>	FeO <sup>a</sup>	MgO	Al <sub>2</sub> O <sub>3</sub>	SiO <sub>2</sub>	CaO	NiO	TiO <sub>2</sub>	V <sub>2</sub> O <sub>5</sub>
44.36	19.71	14.07	10.84	4.54	0.08	0.17	0.27	0.20

<sup>a</sup>FeO: recast as total iron including a small fraction of Fe<sub>2</sub>O<sub>3</sub>

Table 1 represents the chemical composition of the chromite ore of this specific size fraction, based on XRF analysis. XRD analysis (Fig. 2) shows that the chromite ore is mainly composed of chromite, with minor amounts of clinocllore (Mg,Fe)<sub>5</sub>Al(Si<sub>3</sub>Al)O<sub>10</sub>(OH)<sub>8</sub>, magnesite (MgCO<sub>3</sub>) and phlogopite KMg<sub>3</sub>(Si<sub>3</sub>Al)O<sub>10</sub>(OH)<sub>2</sub> as gangue minerals. EDS analysis of a limited number of chromite particles indicates its average composition as (Mg<sub>0.5</sub>-Fe<sub>0.5</sub>)(Cr<sub>1.4</sub>Fe<sub>0.1</sub>Al<sub>0.5</sub>)O<sub>4</sub>. Natural graphite powder of briquetting grade (99.9995% metal basis) in the particle size range of 25–37 μm was used as the reductant. Ni powder of 99.9% purity in the particle size range of 44–75 μm was used as the additive.

### Thermogravimetric analysis

Thermogravimetric analysis was carried out using a NETZSCH STA 449C Simultaneous Thermal Analyzer coupled with a NETZSCH QMS 403C Aeolos Mass Spectrometer, capable of measuring simultaneously the mass change (TG), heat flow (DSC), and off-gas composition (MS). For each test, chromite ore powder was mixed with 25 mass% graphite and/or 20 mass% nickel powders, unless specified otherwise. The well-mixed powder sample of 70 mg was taken and placed into an alumina crucible (O.D. 6.8 mm, volume 85 μL). The sample powder was then pressed inside the crucible followed by placing an

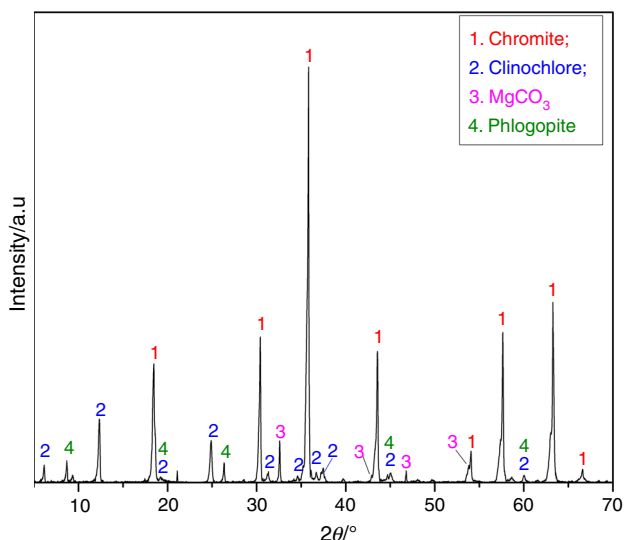


**Fig. 2** XRD pattern of the chromite ore

alumina lid with one pin hole on top of the crucible. The crucible along with a second reference crucible was placed on the sample holder for the TG-DSC-MS measurement.

After closing the top of the TG-DSC, the atmosphere surrounding the crucibles inside the TG-DSC was purged with a vacuum to remove oxygen. A controlled flow of 100 mL min<sup>-1</sup> of argon (5 N) was introduced and maintained as an inert gas for the duration of each test. The sample product from each test was collected for subsequent characterization.

Both the non-isothermal linear heating and isothermal heating tests were performed on the samples in the presence or absence of Ni. Non-isothermal linear heating tests were performed by heating the sample mixture at a fixed heating rate of 15 °C min<sup>-1</sup> up to 1500 °C. Isothermal heating tests were conducted by heating the sample at 20 °C min<sup>-1</sup> to the target temperature followed by dwelling for 180 min.

### Calculation of activation energies

Activation energies were calculated using both isoconversional and model fitting methods. Isoconversional method allows for the observation of the activation energy's dependency on the extent of reduction, while the rate-limiting factor can be determined using the model fitting method [35]. For the calculation of activation energies using isoconversional method, a series of non-isothermal linear heating tests was firstly performed at heating rates of 5, 10, 15 and 20 °C min<sup>-1</sup>. Equation 4 [35] was then employed, in which β represents the heating rate (°C min<sup>-1</sup>), α is the extent of reduction, T is the temperature (K), i denotes the various reduction tests, f(α) represents the dependency of reduction rate (dα/dt) on the extent of reduction (α), A<sub>α</sub> is the preexponential factor (min<sup>-1</sup>) at a specific α, E<sub>α</sub> is the activation energy (kJ mol<sup>-1</sup>) at a specific α, and R is the universal gas constant (i.e., 8.314 × 10<sup>-3</sup> kJ Mol<sup>-1</sup> K<sup>-1</sup>).

A series of isothermal heating tests at varying temperatures ranging from 1300 to 1500 °C were performed before activation energies were calculated using the model fitting method. Calculations of activation energies using this method were based on Eq. 5 [35], in which dα/dt represents the reduction rate (min<sup>-1</sup>), A is the preexponential factor (min<sup>-1</sup>), and E is the activation energy (kJ mol<sup>-1</sup>).

$$\ln \left[ \beta_i \left( \frac{d\alpha}{dT} \right)_{\alpha,i} \right] = \ln [f(\alpha)A_{\alpha}] - \frac{E_{\alpha}}{RT_{\alpha,i}} \quad (4)$$

$$\frac{d\alpha}{dt} = A * \exp \left( \frac{-E}{RT} \right) f(\alpha) \quad (5)$$

## Analytical methods

Powder X-ray diffraction patterns were collected using a Rigaku D/MAX 2500 rotating-anode powder diffractometer with Cu K $\alpha$  radiation at 40 kV, 200 mA. Polished sections of the samples were examined by scanning electron microscope (Hitachi S-3200 N), coupled with energy dispersive spectrometry (Quantax EDS, Bruker) for semi-quantitative analysis with an accelerating voltage of 20 kV.

## Results and discussion

### Non-isothermal linear heating tests

The temperature, mass change, heat flow (DSC) and off-gas analysis results for the non-isothermal linear heating test in the absence of Ni addition are plotted in Fig. 3 as a function of time. The mass change (mg) curve was normalized to represent the test in which the starting sample contained exactly 50 mg chromite ore, among other components (i.e., graphite and/or Ni powder). This normalization method was applied to all other test results in order to allow quantitative comparison of the mass change among different experiments.

As illustrated in Fig. 3, the first thermal event took place in the temperature range between 510 and 740 °C. This endotherm resulted in a mass loss of about 2 mg per 50 mg chromite, and formation of CO<sub>2</sub> and H<sub>2</sub>O as gaseous species. The formation of CO<sub>2</sub> was most likely produced from the thermal decomposition of MgCO<sub>3</sub>, which is present as the magnesite gangue in the chromite ore. This reaction can be represented by the Reaction Eq. 6. FactSage calculation [33] shows the change of Gibbs free energy for this reaction becomes negative when the temperature is above

400 °C, which is in agreement with the temperature range of this thermal event. The formation of H<sub>2</sub>O as one of the gas components is due to the thermal dehydration of clinocllore. The change of Gibbs free energy for this reaction becomes negative when temperature increases to 631 °C [33], which coincides well with the temperature range of this thermal event. Furthermore, Phillips [36] reported that clinocllore dehydrated in the temperature range of approximately 550–700 °C, which further confirms the presence of this thermal event. The second stage mass loss started at about 1140 °C, resulting in a massive endotherm peak (DSC curve), and formation of CO as the main gas species. This endotherm is caused by the carbothermic reduction of chromite by graphite, as represented by Reaction Eqs. 1 to 3. Double-peak appears in both the CO and DSC curves between 90 and 100 min, peaking at 1424 and 1460 °C, respectively. This indicates a multi-stage reduction mechanism that took place.



The results for the non-isothermal linear heating test in the presence of Ni are plotted in Fig. 4, which bears a significant similarity to Fig. 3. Thermal decomposition of MgCO<sub>3</sub> and dehydration of clinocllore also took place in the temperature range of about 510–740 °C. The double-peak also appears during the carbothermic reduction stage at temperatures higher than approximately 1140 °C, peaking at 1421 and 1454 °C, respectively. However, the second endotherm peak became much weaker and sharper, resulting in the disappearance of its corresponding CO peak. Compared with Fig. 3, the most prominent difference is the appearance of an endotherm at 1327 °C, which is likely to have resulted from the melting of the *as-formed* Cr–Fe–Ni alloy as predicted in Fig. 1.

**Fig. 3** Non-isothermal heating of the mixture of chromite and graphite at 15 °C min<sup>-1</sup> in Ar

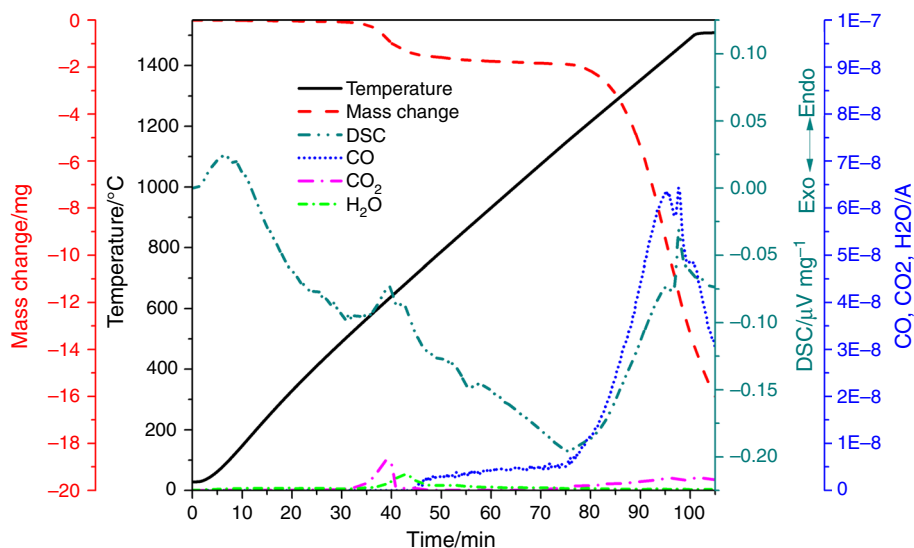
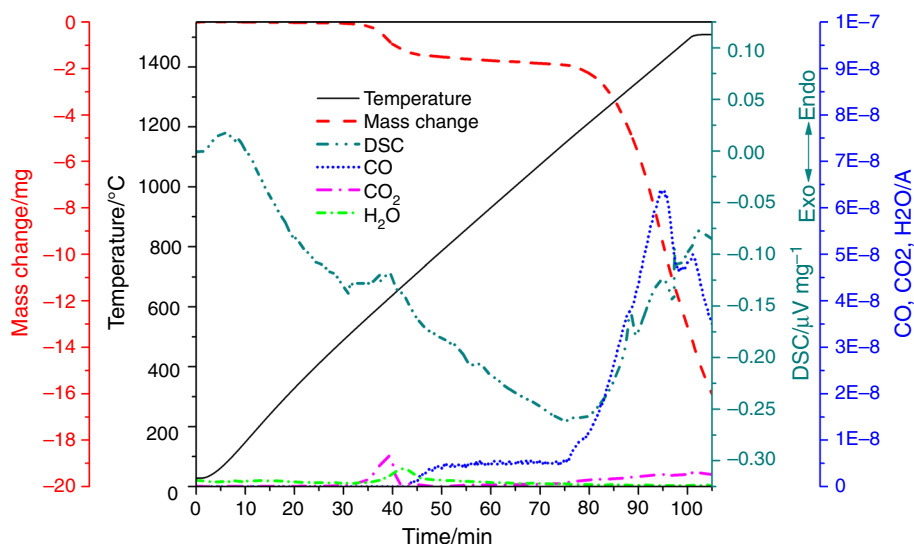


**Fig. 4** Non-isothermal heating of the mixture of chromite, graphite and Ni powder at  $15\text{ }^{\circ}\text{C min}^{-1}$  in Ar



### Isothermal heating at $1400\text{ }^{\circ}\text{C}$ with the variation of Ni addition

Influence of Ni addition in the range of 0–30 wt% was evaluated on the carbothermic reduction of chromite. Degrees of reduction were calculated based on the mass changes for each test, and are plotted in Fig. 5 along with the temperature profile. As can be seen, no significant reduction took place until the temperature increased to above  $1150\text{ }^{\circ}\text{C}$ . Approximately 20% reduction took place before the temperature reached  $1400\text{ }^{\circ}\text{C}$ . The addition of Ni powder affected the reduction slightly negatively in the degree of reduction range of 50–70%. However, limited promoting effect from the Ni addition can be seen at higher degrees of reduction ( $> 70\%$ ). Higher Ni addition has more significant promoting effect, which can be seen from the highest degree of reduction achieved with 30 wt% Ni addition. This acceleration of reduction is probably due to

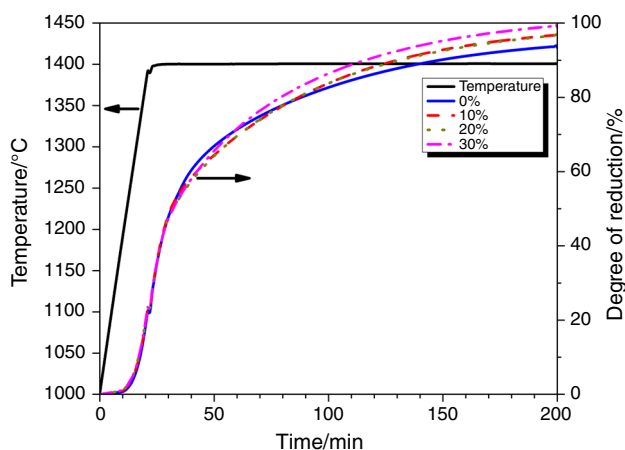


**Fig. 5** Degrees of carbothermic chromite reduction with the variation of Ni addition at  $1400\text{ }^{\circ}\text{C}$

the alloying effect from Ni addition, which effectively lowered the activities of the *as-formed* Cr and Fe metals, and enhanced the mass transfer by forming alloys of lower melting point.

Polished sections of the sample products were examined by SEM and EDS. Figure 6 presents typical morphologies of the reduced products from the tests without Ni addition (a) and with 20 wt% Ni addition (b). In Fig. 6a, the reduced chromite particle is composed of two oxide layers and an alloy core. The outermost layer (A1) is the spinel end-member  $\text{MgAl}_2\text{O}_4$ . The inner oxide layer (A2) is composed of (a) a matrix of mono-oxide (MgO), (b) a Mg–Al–Cr oxide with the  $\text{Mg}/(\text{Al} + \text{Cr})$  ratio being greater than 0.5, and (c) a ferrochrome alloy occurring as small discrete particles. The porous core (A4) is made of a high-Cr ferrochrome alloy. Large FeCr carbide (Cr-rich) particles that are peripheral to the residual chromite particles (e.g., A3) appear to have formed from the direct reduction by the attached graphite particle(s). Similar cross-sectional morphology can be seen from the addition of 20 wt% Ni (Fig. 6b). One significant difference is the presence of relatively large metallic particles composed of Ni-rich alloy (Ni–Fe–Si–Cr) and Cr-rich carbide (Cr–Fe–Ni–C) domains.

### Mechanism of carbothermic chromite reduction at $1400\text{ }^{\circ}\text{C}$

The morphological features of the reduced products illustrated in Fig. 6 indicate the involvement of relatively complex reduction mechanisms. The carbothermic chromite reduction mechanism was therefore further investigated by analyzing the partially reduced products at various reduction degrees. Isothermal tests were performed in the presence of Ni for various time intervals before quickly

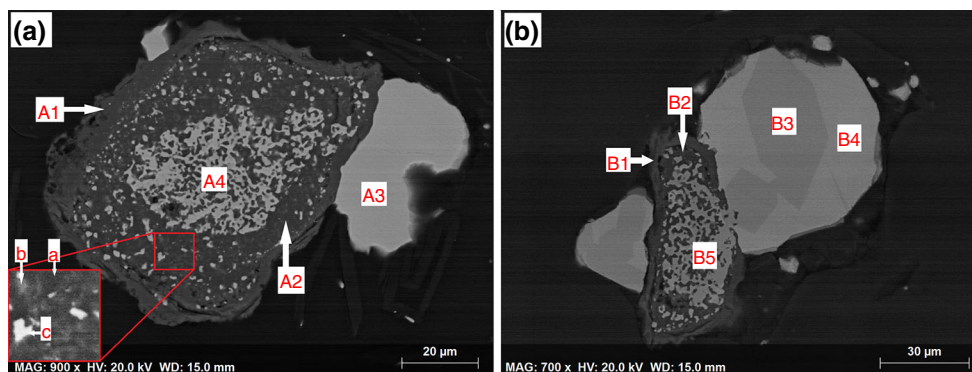


**Fig. 6** Cross sections of the reduced products. **a** No Ni addition; A1:  $\text{MgAl}_2\text{O}_4$ ; A2: (a)  $\text{MgO}$ , (b) an oxide containing Mg, Al, and Cr, and (c) ferrochrome alloy; A3: FeCr carbide (Cr-rich); A4: FeCr alloy

(Cr-rich). **b** 20 mass% Ni addition; B1:  $\text{MgAl}_2\text{O}_4$ ; B2:  $\text{MgO}$  and an oxide containing Mg, Al, and Cr; B3 & B5: Fe–Cr–Ni carbide (Cr-rich); B4: Ni–Fe–Si–Cr alloy (Ni-rich)

cooling down to room temperature, in order to preserve the compositions of the partially reduced products of various reduction degrees. The reduction mechanism was assessed based on the SEM–EDS microanalyses.

Figure 7 presents examples of the cross-sectional morphologies of the partially reduced products of different reduction degrees: (a) 25.7%; (b) 42.6%; (c) 70.3% and (d) 96.8%. Partially reduced products were also subjected

to XRD analysis, with the XRD patterns presented in Fig. 8.

In Fig. 7a representing only 25.7% reduction, shown are two residual chromite particles and a relatively large Ni-rich alloy particle. The reduction resulted in the formation of Cr-rich carbide phase (A2) in the Ni-rich alloy. In the residual chromite particles, the un-reacted core (A3) is surrounded by a reaction rim comprising a large number of

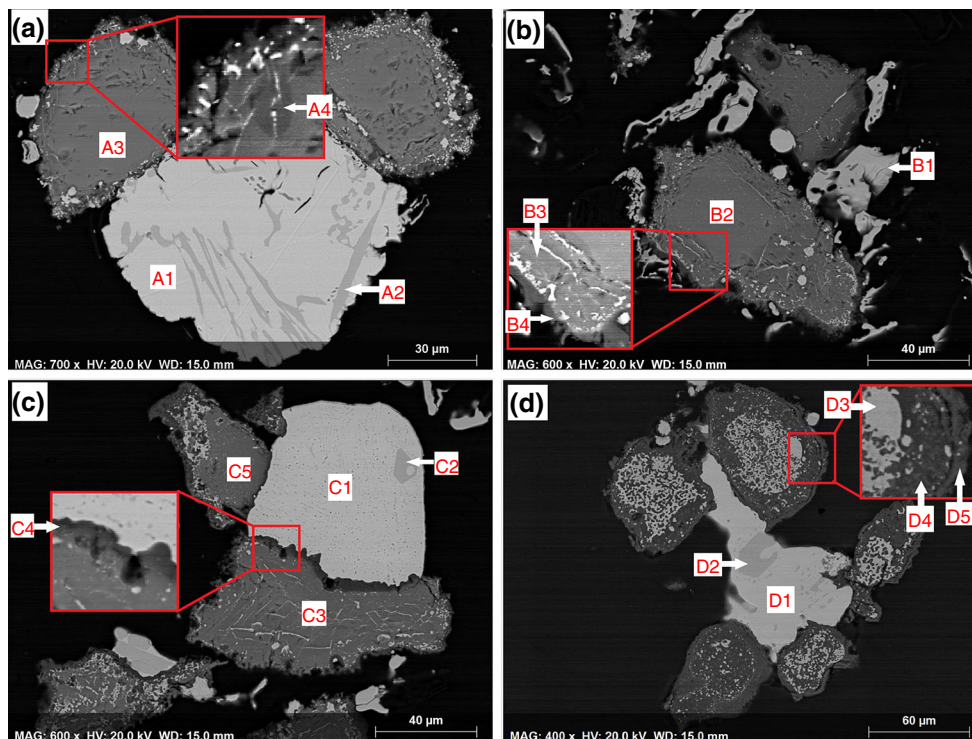


**Fig. 7** Cross sections of the reduced products. **a** 25.7% reduction; A1: Ni–Fe–Cr alloy (Ni-rich); A2: Cr–Fe–Ni carbide (Cr-rich); A3:  $\text{Mg}_{0.5}\text{Fe}_{0.5}\text{Cr}_{1.3}\text{Fe}_{0.1}\text{Al}_{0.6}\text{O}_4$ ; A4:  $\text{Mg}_{0.8}\text{Fe}_{0.2}\text{Cr}_{1.5}\text{Al}_{0.5}\text{O}_4$ . **b** 42.6% reduction, B1: Fe–Cr carbide (Fe-rich); B2:  $\text{Mg}_{0.5}\text{Fe}_{0.5}\text{Cr}_{1.3}\text{Al}_{0.6}\text{Fe}_{0.1}\text{O}_4$ ; B3:  $\text{Mg}_{0.8}\text{Fe}_{0.2}\text{Cr}_{1.4}\text{Al}_{0.6}\text{O}_4$ ; B4:  $\text{Mg}_{0.9}\text{Al}_{1.9}\text{Cr}_{0.1}\text{O}_{4.0}$ ; **c** 70.3% reduction, C1: Ni–Fe–Cr–Si alloy (Ni-rich); C2: Cr–Fe–Ni

carbide (Cr-rich); C3:  $\text{Mg}_{0.9}\text{Fe}_{0.1}\text{Cr}_{1.4}\text{Al}_{0.6}\text{O}_4$ ; C4:  $\text{Mg}_{0.9}\text{Cr}_{0.1}\text{Al}_{2.0}\text{O}_4$ ; C5:  $\text{Mg}_{0.8}\text{Fe}_{0.1}\text{Cr}_{1.5}\text{Al}_{0.6}\text{O}_4$ ; **d** 96.8% reduction, D1: Ni–Fe–Cr–Si alloy (Ni-rich); D2: Cr–Fe–Ni carbide (Cr-rich); D3: Cr–Fe–Ni alloy (Cr-rich); D4:  $\text{MgO}$  and an oxide containing Mg, Al and Cr; D5:  $\text{Mg}_{0.9}\text{Cr}_{0.2}\text{Al}_{1.9}\text{O}_4$

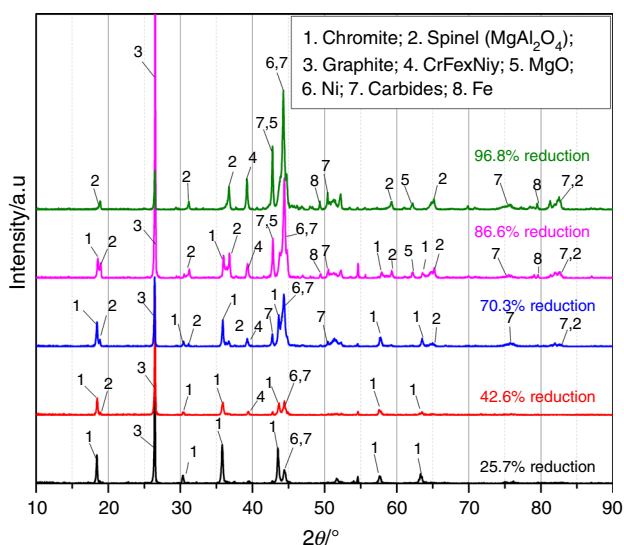


**Fig. 8** XRD patterns of the reduced products of various degrees of reduction

highly disseminated small alloy particles. This suggests that the reduction reactions proceeded to a significant extent via the indirect reactions represented by Reaction Eqs. 1 and 2.

The equilibrium oxygen potential on or near the surface of the chromite particles was likely low enough to allow reduction of Cr ions to a significant extent during the early reduction stage beyond the reduction of  $\text{Fe}^{3+}$  and  $\text{Fe}^{2+}$ . This leads to the formation of a relatively refractory spinel rim B4 (Fig. 7b) with a stoichiometry which is close to  $\text{Mg}_{0.9}\text{Al}_{1.9}\text{Cr}_{0.1}\text{O}_{4.0}$  based on EDS analysis. Compared to the average composition of the original chromite  $(\text{Mg}_{0.5}\text{Fe}_{0.5})(\text{Cr}_{1.4}\text{Fe}_{0.1}\text{Al}_{0.5})\text{O}_4$ , this suggests that all Fe and about 93% Cr have been reduced leaving behind a highly refractory spinel rim. The reduction of both Fe and Cr to a great extent on the surface created surface roughness as shown in Fig. 7b. As seen from XRD analysis (Fig. 8), the refractory spinel ( $\text{MgAl}_2\text{O}_4$ ) started to appear at 42.6% reduction, resulting from the reduction that took place on the chromite surface. Both carbides and Cr-rich alloy can also be identified as the reduction products.

At the early reduction stage, a second zone started to develop beneath the surface layer, represented by A4 in Fig. 7a. Surrounding an Fe-rich alloy whisker, this zone has a stoichiometry of  $(\text{Mg}_{0.8}\text{Fe}_{0.2})(\text{Cr}_{1.5}\text{Al}_{0.5})\text{O}_4$ . Compared to the un-reacted core A3,  $(\text{Mg}_{0.5}\text{Fe}_{0.5})(\text{Cr}_{1.3}\text{Fe}_{0.1}\text{Al}_{0.6})\text{O}_4$ , the compositional change indicates that  $\text{Fe}^{3+}$  is preferentially reduced followed by  $\text{Fe}^{2+}$ , resulting in the formation and growth of the Fe-rich alloy. With increased losses of cations from the spinel structure, both the divalent and trivalent cations would redistribute between the tetrahedral and octahedral sites which may result in inward diffusion of  $\text{Mg}^{2+}$  from the surface layers. As the reduction

proceeded, this transformation continued, indicated in Fig. 7b by the shrinkage of the un-reacted chromite core (B2) and the propagation of the Fe-deficient spinel zone (B3). In Fig. 7c representing the reduction degree of 70.3%, there is no un-reacted or original chromite remaining in the cores.

Continuous reduction of the Fe-deficient spinel zone possibly took place as soon as it was formed, resulting in its even lower Fe concentration. Severe Fe-deficiency eventually led to appreciable Cr reduction. Inside the Fe-deficient zone, further metallization from Cr reduction took place preferably in areas closer to the particle surface beneath the outermost refractory spinel layer because of their lower equilibrium oxygen potential. The refractory spinel formed would continue to grow at the expense of the Fe-deficient chromite. Reduction of  $\text{Cr}^{3+}$  continued until a point after which maintaining the spinel phase was no longer thermodynamically favorable, because of the original  $\text{Mg}^{2+}/\text{Al}^{3+}$  ratio of 1. Accordingly, equal moles of refractory spinel ( $\text{MgAl}_2\text{O}_4$ ) and MgO would have formed as the refractory phases (D4 in Fig. 7) beneath the refractory spinel outer layer. As seen from Fig. 8, formation of MgO was also identified by XRD at higher degrees of reduction ( $\geq 86.6\%$ ). During the last reduction stage, the spinel core was reduced to form the porous alloy core (D3 in Fig. 7) with refractory oxides partially filling the voids.

Influence of Ni addition was also evaluated by EDS multi-point analysis and is plotted in the ternary Cr–Fe–Ni diagram in Fig. 9. Two compositional regions can be identified: Ni-lean region ( $\text{Ni} < 20 \text{ wt}\%$ ) and Cr-lean region ( $\text{Cr} < 20 \text{ wt}\%$ ). Preferential reduction of iron species took place during the early reduction stage, indicated by the formation of high-Fe alloys at 42.6% reduction. It appears that Ni diffused into chromite and formed Ni-

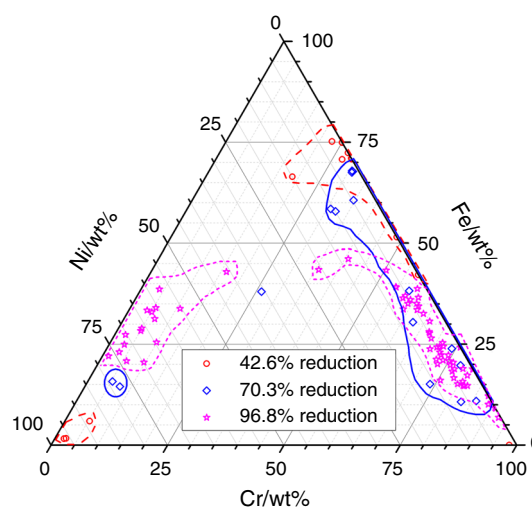


**Fig. 9** Ternary Cr–Fe–Ni composition of the alloys produced from partial reduction at 1400 °C based on EDS point analysis

bearing alloys inside the chromite (e.g., D3 in Fig. 7). In addition, it appears that the Ni particles in contact with chromite particles acted as the metallization sites for both Fe and Cr reduction, resulting in the increasing concentrations of Fe and Cr in the Ni-rich region (or Cr-lean region) as the reduction progressed. Higher concentrations of Cr in the Ni particles resulted in the formation of Cr-rich carbide phase (e.g., A2 and D2 in Fig. 7), as predicted in Fig. 1. Based on Fig. 1, the  $M_7C_3$  carbide formed generally has Ni concentrations of no greater than about 10 wt%, which is in good agreement with the EDS measurement on the carbide as shown in the Ni-lean region.

### Effect of reduction temperature

A series of reduction tests were performed at various isothermal temperatures in the absence of Ni addition. As illustrated in Fig. 10, much higher degrees of reduction can be achieved at higher reduction temperatures. Compared to the early reduction stage (e.g., < 30 min), later stages of reduction become significantly slower because of the formation and growth of a relatively refractory spinel layer on the surfaces of chromite and the mono-oxide matrix (MgO) layer beneath it.

Figure 11 illustrates the results from isothermal reduction tests in the presence of Ni. Consistently, higher reduction temperature leads to a higher degree of reduction. In comparison with the isothermal tests without Ni (Fig. 10), the addition of Ni has a slightly negative influence on the carbothermic reduction of chromite at 1300 °C. This indicates that the alloying effect from adding Ni is not as significant at lower temperatures, partially because of the fewer amounts of molten alloys formed. Overall, the positive alloying effect was not significant enough to overcome the negative diluting effect from adding Ni. At

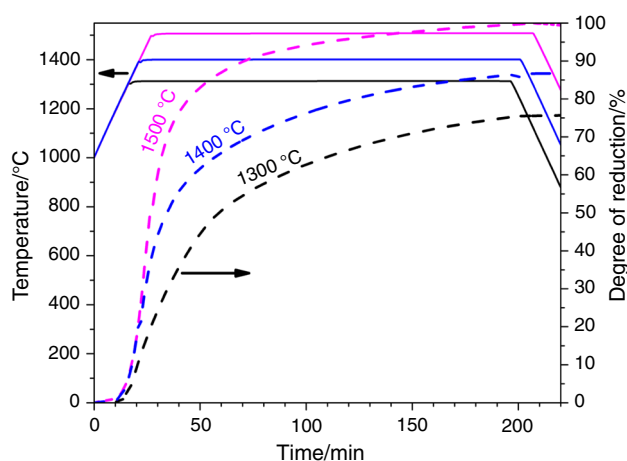


**Fig. 10** Degrees of carbothermic reduction of chromite without addition of Ni at various reduction temperatures

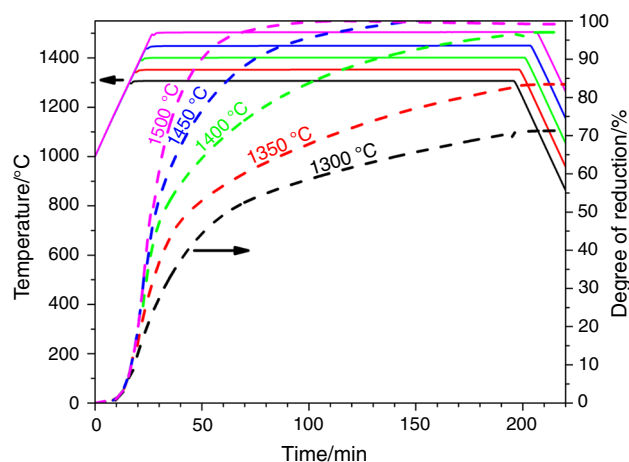


**Fig. 11** Degrees of carbothermic reduction of chromite with the addition of 20 wt% Ni at various reduction temperatures

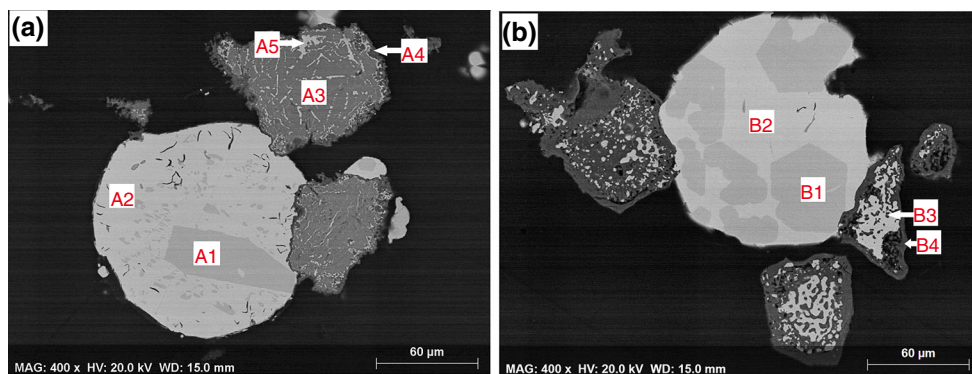
temperatures higher than 1300 °C, the carbothermic reduction of chromite was significantly promoted with Ni addition.

Figure 12 illustrates the morphologies of the products from reduction at 1300 °C (a) and 1500 °C (b). In Fig. 12a, two partially reduced chromite particles were attached to a Ni-rich alloy. The reduction of Cr caused the formation of Cr-rich carbide phases (A1) inside the Ni-rich NiFeCrSi alloy (A2). Partial reduction at 1300 °C resulted in the preferential reduction of iron, evidenced by the presence of Fe-deficient chromite core A3 with the stoichiometry of  $(Mg_{0.9}Fe_{0.1})(Cr_{1.4}Al_{0.6})O_4$ . Metallization also took place inside the chromite particles, forming Fe-rich FeCrNi alloys (A5). The Fe-deficient chromite core was surrounded by a relatively refractory spinel (A4). At 1500 °C, the reduction was near complete, leading to the formation of higher proportions of Cr-rich carbide (B1) in the Ni-rich alloy particles (B2). The refractory spinel phase (B4) still contains minor amounts of Cr.

### Calculation of activation energies

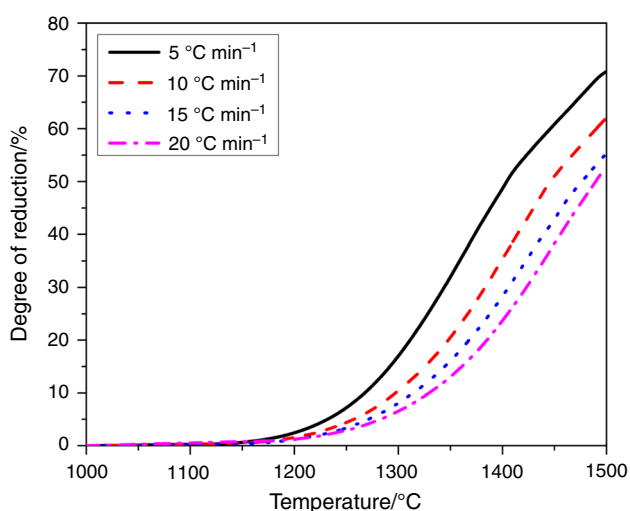
#### Isoconversional method

The degrees of chromite reduction in the absence of Ni at various linear heating rates are plotted against temperature in Fig. 13. As can be seen, no appreciable amounts of reduction took place below 1100 °C in all four tests. Slower heating rate resulted in higher degrees of reduction, because of more time allowed for reduction at each temperature at a slower heating rate. Equation 4 [35] was employed for the calculation of apparent activation energies. The linear relationships at each  $\alpha$  ranging from 0.05 to 0.60 with an interval of 0.05 are plotted in Fig. 14 as an inset, by re-processing the data presented in Fig. 13.



**Fig. 12** Cross sections of the reduced products. **a** reduced at 1300 °C; A1: CrFeNi carbide (Cr-rich); A2: NiFeCrSi alloy (Ni-rich); A3:  $(\text{Mg}_{0.9}\text{Fe}_{0.1})(\text{Cr}_{1.4}\text{Al}_{0.6})\text{O}_4$ ; A4:  $\text{Mg}_{0.9}\text{Cr}_{0.4}\text{Al}_{1.7}\text{O}_4$ ; A5: FeCrNi alloy

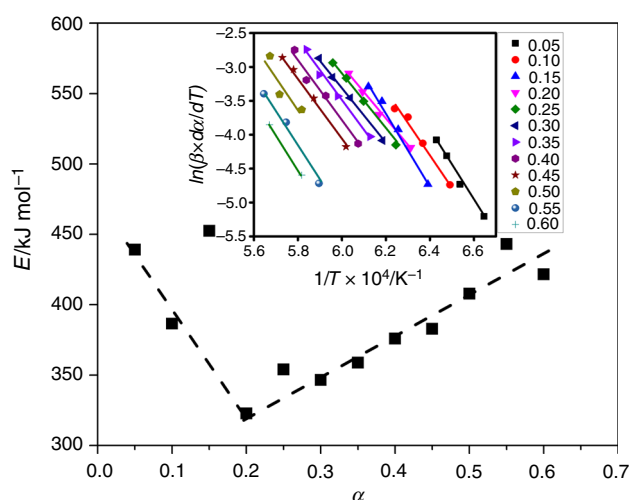
(Fe-rich). **b** reduced at 1500 °C; B1: CrFeNi carbide (Cr-rich); B2&B3: NiFeCrSi alloy (Ni-rich); B4:  $\text{Mg}_{0.9}\text{Cr}_{0.2}\text{Al}_{1.9}\text{O}_4$



**Fig. 13** Carbothermic reduction of chromite at constant heating rates up to 1500 °C

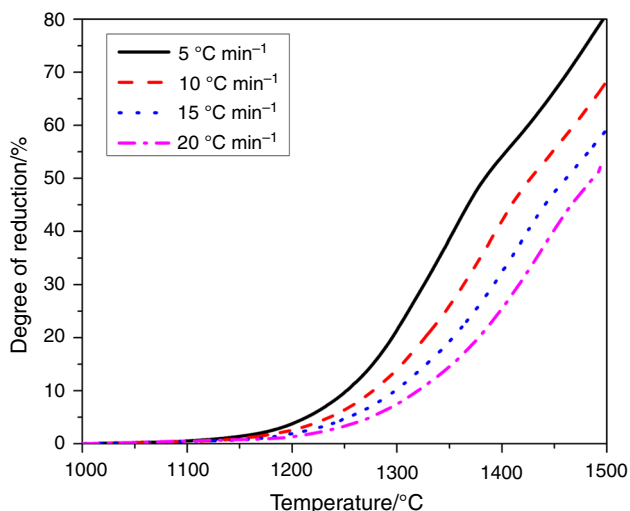
Apparent activation energies were calculated based on their slopes and are presented in Fig. 14. A decreasing trend is seen in the lower  $\alpha$  range from 0.05 to 0.20. The apparent activation energy drops from 452 to 323  $\text{kJ mol}^{-1}$  in this relatively narrow  $\alpha$  range, indicating a quick transition of rate-controlling mechanisms. A gradual and relatively linear increase in the apparent activation energy in the  $\alpha$  range of 0.20 to 0.60 demonstrates that the reduction rate is mix-controlled. The heavy dependency of the apparent activation energy on the extent of reduction reveals the relatively complex nature of the carbothermic chromite reduction.

Figure 15 shows the degrees of chromite reduction in the presence of Ni at different linear heating rates. For the calculation of apparent activation energies, the same data processing method was employed by firstly identifying the linear relationships between  $\ln(\beta \times d\alpha/dT)$  and  $1/T$  for each extent of reduction ( $\alpha$ ), which are illustrated in Fig. 16 as an inset. The apparent activation energies were then



**Fig. 14** Calculated apparent activation energies as a function of the extent of reduction using the differential isoconversional method.  $\ln(\beta \times d\alpha/dT)$  versus  $1/T$  at various extent of reduction ( $\alpha$ ) is also plotted as an inset

calculated based on their slopes and plotted in Fig. 16 as a function of  $\alpha$ . Similarly, a quick drop of the apparent activation energy from 458 to 254  $\text{kJ mol}^{-1}$  can be seen at the early reduction stage ( $0.05 \leq \alpha \leq 0.15$ ), followed by a linear gradual increase from 254 to 322  $\text{kJ mol}^{-1}$  in the  $\alpha$  range of 0.15–0.45. The activation energy increased at a higher rate from 299  $\text{kJ mol}^{-1}$  up to 450  $\text{kJ mol}^{-1}$  in the later stage reduction ( $0.5 \leq \alpha \leq 0.65$ ). These three trends in the change of activation energy represent three stages of reduction, each with its own rate-controlling mechanism. The promotion effect on the carbothermic chromite reduction from adding Ni can also be revealed by comparing the change of activation energies with and without the presence of Ni. The lowest activation energy is 323  $\text{kJ mol}^{-1}$  at  $\alpha = 0.2$  without Ni addition (Fig. 14), while it is reduced to 254  $\text{kJ mol}^{-1}$  at  $\alpha = 0.15$  (Fig. 16) in the presence of 20 mass% Ni. Its effectiveness in



**Fig. 15** Carbothermic reduction of chromite with 20 wt% Ni addition at constant heating rates up to 1500 °C

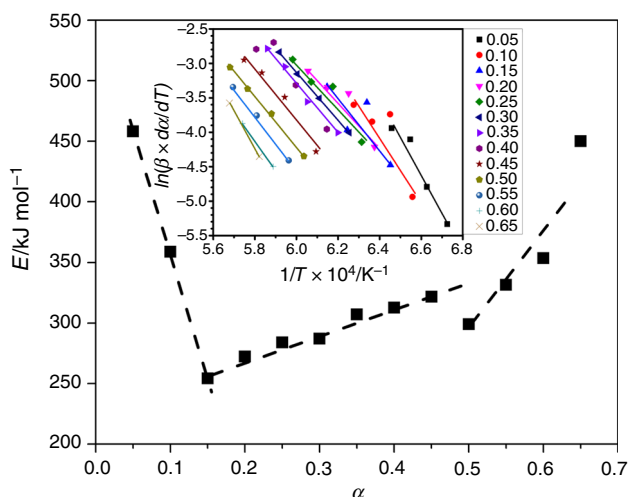


**Fig. 16** Calculated activation energies as a function of the extent of reduction using the differential isoconversional method for the tests with Ni addition.  $\ln(\beta \times d\alpha/dT)$  versus  $1/T$  at various extent of reduction ( $\alpha$ ) is also plotted as an inset

promoting the carbothermic reduction by lowering the activation energy can be seen in the wide range of  $\alpha$  from 0.1 to 0.6.

**Model fitting method**

Degrees of reduction from the series of isothermal heating tests in the presence of Ni (Fig. 11) were used for the calculation of activation energies, based on Eq. 5 [35]. It should be noted that only the isothermal regions can be used for model fitting (Fig. 11). As a result, early reduction stage ( $\alpha < 0.1$ ) cannot be evaluated because of the lack of data. In the  $\alpha$  range of 0.1–1.0, two regions were identified when performing the model fitting operations, separated by

the  $\alpha$  of about 0.56. Model R3 (Eq. 7) [35] was found to fit best in the  $\alpha$  range of 0.1–0.56, with the fittings plotted in Fig. 17 as an inset. This model means the reduction kinetics is controlled by chemical reaction(s). Its corresponding Arrhenius plot is shown in Fig. 17, with the calculated apparent activation energy of 213 kJ mol<sup>-1</sup>, and the preexponential factor (A) of  $1.90 \times 10^5 \text{ min}^{-1}$ . Model D3 (Eq. 8) [35] fits best to the experimental data when  $\alpha$  is within 0.56 and 1.00. The linear fits are shown in Fig. 18 as an inset. This D3 model indicates that the carbothermic reduction is controlled by diffusion within chromite particles in this  $\alpha$  range of investigation. Apparent activation energy, calculated based on the slope of the Arrhenius plotting (Fig. 18), is 345 kJ mol<sup>-1</sup>, with the preexponential factor of  $1.38 \times 10^8 \text{ min}^{-1}$ .

$$f(\alpha) = 3 * (1 - \alpha)^{2/3} \tag{7}$$

$$f(\alpha) = 3/2 * (1 - \alpha)^{2/3} * [1 - (1 - \alpha)^{1/3}]^{-1} \tag{8}$$

Relating to the reduction mechanisms discussed in Sect. “Mechanism of carbothermic chromite reduction at 1400 °C”, the  $\alpha$  range of 0.1–0.56 represents the reduction stage in which preferential Fe reduction was still dominating, and the refractory double-oxide-layer was not well developed. The reduction kinetics was therefore predominantly limited by reduction reactions with the apparent activation energy of 213 kJ mol<sup>-1</sup>. As the reduction progressed to higher degrees ( $0.56 < \alpha < 1.00$ ), the refractory oxide double-layer on the surface of each chromite particle became appreciably thick, and Cr reduction became dominating. This change led to the shift of rate-limiting mechanism from chemical control to diffusion control, with a higher apparent activation energy of 345 kJ mol<sup>-1</sup>. This coincides very well with the multi-stage reduction

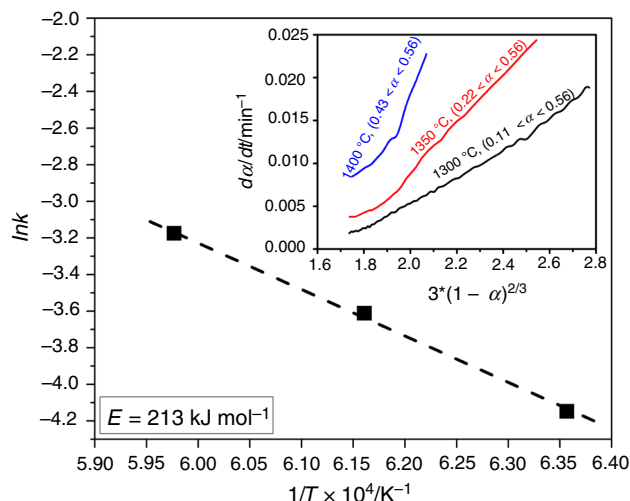


**Fig. 17** Arrhenius plot for the reaction model R3. Rate of reduction ( $d\alpha/dt$ ) versus  $3*(1 - \alpha)^{2/3}$  is also plotted as an inset

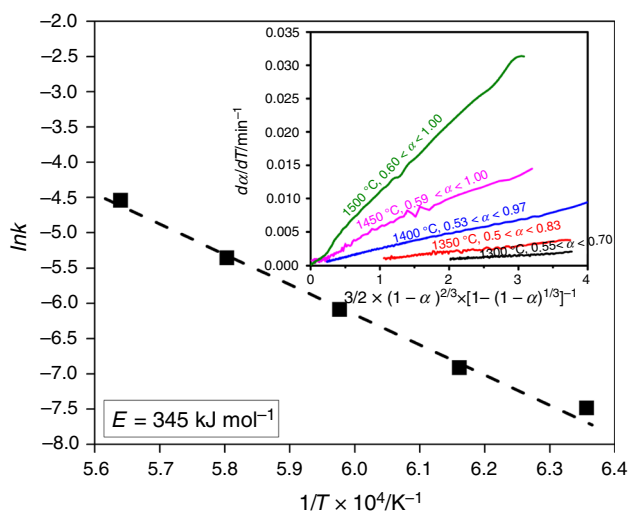


**Fig. 18** Arrhenius plot for the reaction model D3. Rate of reduction ( $d\alpha/dt$ ) versus  $3/2 \times (1 - \alpha)^{2/3} \times [1 - (1 - \alpha)^{1/3}]^{-1}$  is also plotted as an inset

mechanism indicated by the dependency of apparent activation energy on the reduction extent (Fig. 16). Figure 16 also indicates a third rate-limiting step at the very early stage of reduction ( $\alpha < 0.1$ ). This rate-limiting step is probably represented by the nucleation of alloys inside the chromite particles closer to the surface, as indicated by the large number of newly formed alloy beads located around the edge of chromite particles (Fig. 7a).

## Conclusions

Kinetics and mechanisms of the carbothermic reduction of chromite with and without the addition of Ni powder were investigated by thermogravimetric analysis coupled with continuous off-gas measurements (TG-DSC-MS). The results indicate that the thermal dehydration of clinocllore and decomposition of magnesite took place in the temperature range of 510–740 °C. No appreciable carbothermic reduction of chromite took place below about 1100 °C.

Three stages of reduction were identified with the addition of Ni powder. The first stage reduction ( $\alpha < 0.1$ ) was characterized by its high apparent activation energy, which is in the vicinity of 450 kJ mol<sup>-1</sup>. The main reductions took place on or near the surface of the chromite particles, resulting in the nucleation of disseminated alloy beads in the reaction zone close to the particle surface. During the early stages of reduction, chromite particle surfaces were exposed to a reducing atmosphere with extremely low oxygen potential. This led to the reduction of both Fe and Cr from near the particle surfaces, forming a thin layer of refractory spinel (MgAl<sub>2</sub>O<sub>4</sub>). The second reduction stage ( $0.1 < \alpha < 0.65$ ) involved preferential Fe

reduction with the inward propagation of the Fe-deficient chromite zone, during which the rate of reduction was mainly controlled by chemical reactions. Considerable Cr reduction took place as soon as the local Fe concentration dropped to a certain level, which gradually progressed inwards toward the chromite core. Inward continuous growth of the surface spinel layer continued until the formation of spinel was no longer thermodynamically favorable. At this point, MgO began to form as one of the refractory oxides beneath the spinel layer. Continuous growth of this double-oxide-layer, as the reduction progressed, initiated the third stage of reduction ( $\alpha > 0.65$ ), during which the reduction rate is no longer controlled by chemical reactions. Instead, diffusion through this refractory double-oxide-layer became the rate-limiting step, with the apparent activation energy of 345 kJ mol<sup>-1</sup>.

The promoting effect of Ni addition was evident at temperatures higher than 1300 °C. Its alloying effect took place by absorbing Fe and Cr from adjacent chromite particles and forming alloys of low melting point. Enrichment of Cr in the alloy resulted in the formation of Cr-rich carbide in the molten Ni-rich alloy. It appears that Ni diffused into chromite to form Ni-bearing alloys embedded in the chromite particles. Its alloying effect reduced the apparent activation energy of carbothermic chromite reduction by approximately 70 kJ mol<sup>-1</sup>.

**Acknowledgements** The following contributions are acknowledged: Judith Price for the preparation of polished sections, Derek Smith for XRD analyses, Elizabeth Houghton and Khushmeet Gill for SEM analyses, and KWG Resources Inc. for providing the ore samples. The study was funded by NRCan under the Rare Earth Elements and Chromite R&D Program.

## References

- Slatter DD. Technological trends in chromium unit production and supply. INFACON 7; FFF, Trondheim, Norway; 1995. p. 249–62.
- Murthy YR, Tripathy SK, Kumar CR. Chrome ore beneficiation challenges & opportunities—a review. Miner Eng. 2011;24:375–80.
- Johnson J, Reck BK, Wang T, Graedel TE. The energy benefit of stainless steel recycling. Energy Policy. 2008;36:181–92.
- Chakraborty D, Ranganathan S, Sinha SN. Investigations on the carbothermic reduction of chromite ores. Metall Mater Trans B. 2005;36B:437–44.
- Niyesh MJ, Dippenaar RJ. The solid state reduction of chromite. In: INFACON 6. Proceedings of the 6th international ferroalloy congress, Cape Town, South Africa; 1992. p. 57–63.
- Ding YL, Warner NA. Kinetics and mechanism of reduction of carbon-chromite composite pellets. Ironmak Steelmak. 1997;24(3): 224–9.
- Perry KPD, Finn CWP, King RP. An ionic diffusion mechanism of chromite reduction. Metall Trans B. 1988;19B:677–84.
- Roschin AV, Karnoukhov VN, Roschin VE, Malkov NV. New findings in research of solid phase reactions in chromite ore reduction processes. In: Proceedings: tenth international ferroalloys congress, Cape Town, South Africa; 2004. p. 333–42.

9. Atasoy A, Sale FR. An investigation on the solid state reduction of chromite concentrate. *Solid State Phenom.* 2009;147–149:752–7.
10. Murti NSS, Seshadri V. Kinetics of reduction of synthetic chromite with carbon. *Trans ISIJ.* 1982;22:925–33.
11. Soykan O, Eric RH, King RP. The reduction mechanism of a natural chromite at 1416 °C. *Metall Trans B.* 1991;22B:53–63.
12. Wang Y, Wang L, Xu J, Chou KC. Kinetics of carbothermic reduction of synthetic chromite. *J Min Metall Sect B Metall.* 2014;50(1):15–21.
13. Hu X, Okvist LS, Yang Q, Bjorkman B. Thermogravimetric study on carbothermic reduction of chromite ore under non-isothermal conditions. *Ironmak Steelmak.* 2015;42(6):409–16.
14. Nafziger RH, Tress JE, Paige JI. Carbothermic reduction of domestic chromites. *Metall Trans B.* 1979;10B:5–14.
15. Kekkonen M, Xiao Y, Holappa L. Kinetic study on solid state reduction of chromite pellets. In: *INFACON 7*, Trondheim, Norway; 1995. p. 351–60.
16. Dawson NF. The solid state reduction of chromite (PhD thesis). Durban: University of Natal; 1989.
17. Dawson NF, Edwards RI. Factors affecting the reduction of chromite. Reio De Janeiro, Barzil: *INFACON*; 1986. p. 1–11.
18. Zhao B, Hayes PC. Effects of oxidation on the microstructure and reduction of chromite pellets. In: *The twelfth international ferroalloys congress (INFACON XII)*, Helsinki, Finland; 2010. p. 263–73.
19. Kleynhans ELJ, Neizel BW, Beukes JP, Zyl PGV. Utilisation of pre-oxidized ore in the pelletised chromite pre-reduction process. *Miner Eng.* 2016;92:114–24.
20. Ding YL, Warner NA. Catalytic reduction of carbon-chromite composite pellets by lime. *Thermochim Acta.* 1997;292:85–94.
21. Apaydin F, Atasoy A, Yildiz K. Effect of mechanical activation on the carbothermal reduction of chromite with metallurgical coke. *Can Metall Q.* 2011;50(2):113–8.
22. Lekatou A, Walker RD. Effect of SiO<sub>2</sub> addition on solid state reduction of chromite concentrate. *Ironmak Steelmak.* 1997;24(2):133–43.
23. Weber P, Eric RH. Solid-state fluxed reduction of LG-6 chromite from the Bushveld complex. In: *INFACON 6*. Proceeding of the 6th international ferroalloys congress, Cape Town, South Africa; 1992. p. 71–7.
24. Weber P, Eric RH. The reduction mechanism of chromite in the presence of a silica flux. *Metall Trans B.* 1992;24(6):987–95.
25. Weber P, Eric RH. The reduction of chromite in the presence of silica flux. *Miner Eng.* 2006;19:318–24.
26. Duong HV, Johnston RF. Kinetics of solid state silica fluxed reduction of chromite with coal. *Ironmak Steelmak.* 2000;27(3):202–6.
27. Deventer JSJV. The effect of additives on the reduction of chromite by graphite: an isothermal kinetic study. *Thermochim Acta.* 1988;127:25–35.
28. Hu X, Teng L, Wang H, Okvist LS, Yang Q, Bjorkman B, et al. Carbothermic reduction of synthetic chromite with/without the addition of iron powder. *ISIJ Int.* 2016;56(12):2147–55.
29. Hu X, Wang H, Teng L, Seetharaman S. Direct chromium alloying by chromite ore with the presence of metallic iron. *J Min Metall Sect B Metall.* 2013;49(2):207–15.
30. Hu X, Yang Q, Okvist LS, Bjorkman B. Thermal analysis study on the carbothermic reduction of chromite ore with the addition of mill scale. *Steel Res Int.* 2015;86:1–9.
31. Yape EO. Fe–Ni–Cr crude alloy production from direct smelting of chromite and laterite ores. *J Med Bioeng.* 2014;3(4):245–50.
32. Katayama HG, Tokuda M, Ohtani M. Promotion of the carbothermic reduction of chromite ore by the addition of borates. *Iron Steel Inst Jpn.* 1986;72(10):1513–20.
33. Bale CW, Belisle E, Chartrand P, Decterov SA, Eriksson G, Gheribi AE, et al. *FactSage Thermochemical Software and Database*, 2010–2016. *Calphad.* 2016;54:35–53.
34. Dresler W, McLean A. The extraction of ferrochromium in the presence of nickel from bird river chromite ores. *Can Metall Q.* 1992;31(3):181–8.
35. Vyazovkin S, Burnham AK, Criado JM, Pérez-Maqueda LA, Popescu C, Sbirrazzuoli N. ICTAC Kinetics Committee recommendations for performing kinetic computations on thermal analysis data. *Thermochim Acta.* 2011;520(1–2):1–19. <https://doi.org/10.1016/j.tca.2011.03.034>.
36. Phillips WR. A differential thermal study of the chlorites. *Mineral Mag.* 1963;33(260):404–14.